Mechanical Engineering Faculty Publications
Mechanical Engineering

1-2013

Investigation of Turbulent Structure Modification by Momentum Injection Into Turbulent Flow Over a Rough Surface

Mark A. Miller
University of Kentucky

Huaibao Zhang
University of Kentucky, paulhuaizhang@uky.edu

Alexandre Martin
University of Kentucky, alexandre.martin@uky.edu

Sean C. C. Bailey
University of Kentucky

Right click to open a feedback form in a new tab to let us know how this document benefits you.

Investigation of Turbulent Structure Modification by Momentum Injection Into Turbulent Flow Over a Rough Surface

Notes/Citation Information

Published in the *Proceedings of the 51st AIAA Aerospace Sciences Meeting including the New Horizons Forum and Aerospace Exposition*, Paper 2013-0534, p. 1-10.

51st AIAA Aerospace Sciences Meeting including the New Horizons Forum and Aerospace Exposition
07 - 10 January 2013, Grapevine (Dallas/Ft. Worth Region), Texas

AIAA 2013-0534

Investigation of Turbulent Structure Modification by Momentum Injection Into Turbulent Flow Over a Rough Surface

Mark A. Miller,* Huai-Bao Zhang,*

Alexandre Martin† and Sean C. C. Bailey‡

Department of Mechanical Engineering, University of Kentucky, Lexington, KY, 40506, USA

Utilizing a turbulent channel flow facility, experiments were performed to determine the modifications made to the temporal and spatial structure of turbulence over a sinusoidally rough surface due to momentum injection through the surface. As expected, when compared to the smooth-walled conditions, it was found that the surface roughness increased wall shear stress, decreased the turbulence energy content near the wall, and shifted that energy content to wavelengths on the order of the roughness elements. The addition of momentum injection was found to produce further modifications analogous to increasing the roughness height by increasing the wall shear stress and further reducing the energy content of the near-wall turbulence while simultaneously shifting it to longer wavelengths.

Nomenclature

Symbols

ρ	Density, kg/m^3	d	Zero plane displacement, m
h	Channel half height, m	k_s	Equivalent sand grain roughness, m
ν	Kinematic viscosity m^2/s	ΔU^+	Roughness function
x	Streamwise direction	f	Frequency, Hz.
y	Wall normal direction	λ	Wavelength, m
D	Pipe diameter, m	k	Wavenumber, 1/m
p	Pressure, Pa	ϕ_{uu}	Streamwise power spectral density
$\langle U \rangle$	Area averaged velocity, m/s		
$\overline{u'^2}$	Turbulence intensity, m/s	*Subscripts*	
R_{e_h}	Reynolds number based on half height		
R_{c_τ}	Reynolds number based on friction velocity	cl	Channel centerline
k_r	Roughness Reynolds number	inj	Injected flow characteristic
c_f	Coefficient of friction	x	Property of streamwise direction
K	Pressure loss coefficient	$\mid$	Scaling with friction velocity

Overbar indicates time average

I.   Introduction

Ablative materials for use in thermal protection systems (TPS) have a very successful track record as an effective heat shield material when the most demanding re-entry conditions are encountered. Ablative TPS systems can be divided into two types: charring (or pyrolizing) and non-charring. The principle behind the use of charring ablators is simple: energy absorbed through removal of material from the surface is not used

---

*Graduate Research Assistant, Mechanical Engineering, AIAA Student Member
†Assistant Professor, Mechanical Engineering, AIAA Member.
‡Assistant Professor, Mechanical Engineering.

to heat the TPS, therby keeping it at a lower temperature. In the case of charring ablators, the ablative material is a resin that fills the pores of a carbon matrix. Although the matrix might ablate, it usually does not, thus producing an aerodynamic surface consisting of a sparse, porous geometry during re-entry.

Many physical phenomena occur during ablation of a TPS which must be modeled correctly when designing re-entry systems. For example, pyrolysis chemistry within the TPS and the flow of pyrolysis gas through the porous surface. The near-wall flow field is affected by the chemical species emitted from the ablating surface and injected into the near-wall flow. The presence of this ablation gas greatly reduces the heat flux on the vehicle by: (1) thickening the thermal boundary layer and reducing the temperature gradient near the wall; (2) changing the gas composition near the wall which triggers chemical reactions; and (3) injection a relatively cooler gas into the flow field. The complexity of the processes which must be modeled leads to uncertainty when designing a TPS and requires generous margins of safety. Furthering our understanding of pyrolizing ablator physics has the potential to lead to improve the safety of TPS designs while reducing launch costs through weight reduction.

The key element in a properly functioning charring ablator is the flow of pyrolysis gases from the surface into the boundary layer. Any modeling effort concerning the design of ablative material TPS must therefore take into account flow injection and its effect on the heat flux to the vehicle. Additionally, the TPS surface geometry must be accurately modeled, which is complicated by roughening of the char surface and possible material removal by thermomechanical erosion.[5] This roughness also introduces disturbances in the flow field which can lead to transition to turbulence, particularly for larger TPS surfaces. Turbulent flow over a TPS surface will drastically increase the transport of mass, momentum and energy between the surface and the flow field and therefore improving our ability to model the turbulent physics of the near-wall flow during charring ablation is crucial to understanding these transport processes.

Extensive work has been completed on roughness induced turbulence,[6,11,14,15,21,25] although there is still no methodology for predicting turbulent flow behavior over an arbitrary surface roughness topology.[24] There has also been extensive work performed on turbulent transition where flow injection is present.[22,23] Surprisingly, however, there have been very few studies combining both the effects of blowing and of roughness on turbulent boundary layers.[28] The current set of experiments aim to improve our understanding of how these two parameters modify the structure of turbulent flow forming over the surface.

Here we present results from an experiment conducted in a turbulent channel flow wind tunnel to investigate the near-wall turbulence over a sinusoidally rough, micro-perforated surface, both with and without flow injection through the surface. These measurements are believed to be the first quantification of turbulence statistics for flows combining the effects of both roughness and blowing.

Experiment Description

The experiments were performed in the Turbulent Channel Flow Facility (TCFF) at the University of Kentucky's Experimental Fluid Dynamics Laboratory (EFDL). The TCFF has been carefully designed to produce fully developed turbulent, plane Poiseuille flow at centerline flow velocities of up to $U_{cl} = 45m/s$ corresponding to a maximum Reynolds number based on half height of $R_{c_h} = hU_{cl}/\nu = 150,000$, where ν is the kinematic viscosity and h is the channel half-height of $h = 0.0508m$. The channel has an aspect ratio of 9:1 to ensure quasi-2D flow at the centerline[29]. The distance from the channel inlet to the test section is $280h$, allowing the turbulence to reach a fully-developed state naturally[17] before entering the channel test section, $246h$ downstream of the inlet.

For this set of experiments, a $24h$ long section of the smooth-walled test section roof was replaced by a nominally two-dimensional, sinusoidally varying rough surface with a streamwise wavelength of $\lambda = 7$ mm and an amplitude of 0.4 mm pictured in Fig. 1. This surface is micro-perforated to allow for additional injection of gases into the test section. Flow is driven through the surface by ten 14 W Sofasco SF12038 high-flow fans which pressurize the upper plenum of the blowing apparatus (Fig. 2). The blowing apparatus is further equipped with two lower sections, separated by screens and flow straightening honeycombs, designed to break down large-scale disturbances introduced by the fans. This ensures an even, laminar injection of air across the rough surface. The first screen is composed of a 3 mm square mesh and the flow is allowed to decay 203 mm before reaching the flow straightener. The straightener is formed of thin aluminum strips bonded in a honeycomb matrix. The flow travels 50 mm through the straightener and past the second screen of square mesh size 1.5 mm. Finally, the flow decays an additional 100 mm before reaching the rough surface.

In order to characterize the injection rate into the test section from the blowing apparatus, the blowing

American Institute of Aeronautics and Astronautics
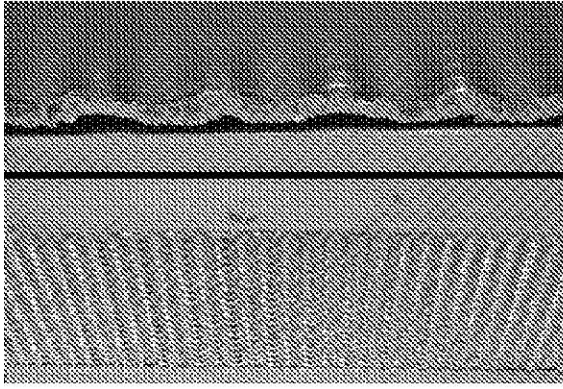
Figure 1. *Sinusoidal surface roughness with micro-cracked pores visible*
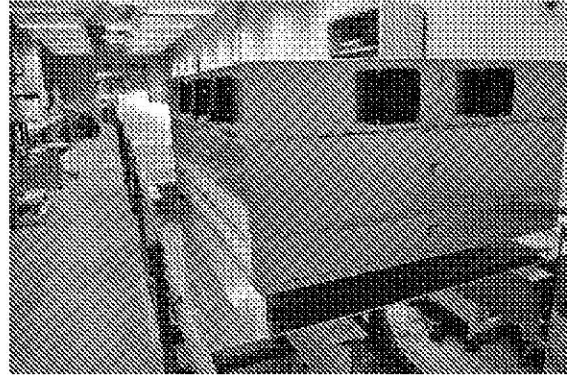
Figure 2. *Blowing apparatus mounted above test section of TCFF*

ratio BR was defined as

$$BR = \frac{(\rho U)_{inj}}{(\rho U)_{cl}} \tag{1}$$

where U_{inj} indicates the average velocity of the flow injected through the surface and U_{cl} the mean centerline velocity. To determine BR, the blowing rig was designed with eight pressure taps located circumferentially around the blowing apparatus in sets of four. One set is located midway between the flow conditioning screens and the second set is located between the bottom screen and the rough surface. The bottom set of taps, together with a measurement of the static pressure in the channel test section are used to determine the mean injected flow velocity using the loss coefficient

$$K = \frac{\Delta p}{1/2 \rho U_{inj}^2} \tag{2}$$

where Δp the measured pressure drop across the screen.[26] The value of K for the test surface provided a novel way of determining the very low flow rates experienced through the rough surface and was determined through a separate set of experiments conducted in a pipe flow facility constructed specifically to determine K. The pipe was constructed of smooth PVC, with a diameter, $D = 50.8$ mm. The pipe was pressurized at one end and the flow rate regulated via a ball valve. The flow entered the pipe and was allowed to develop along a length of $295D$ before entering the test section. The insertion of a porous test specimen was performed with specially designed plugs which positioned the test specimen in the pipe but did not allow for pressurized air to escape the pipe. This test section was followed by a further $100D$ of pipe to allow for pressure measurements after the test article. The pipe was fitted with pressure taps[26] which allowed for determination of the pressure drop across the test article and along the pipe section. The velocity profile at the pipe outlet was also measured using a Pitot-static tube mounted on a traverse. To characterize K, the inlet pressure was varied and the the pressure drop across the sample and mean exit velocity were recorded.

Turbulence measurements were conducted in the TCFF at 40 wall-normal positions inside the channel using a single-component hot-wire anemometer (HWA) due to its ability to temporally resolve the streamwise turbulent fluctuations. The HWA probes were operated at an overheat ratio of 1.6, resulting in a measured square-wave response above 70 kHz. The anemometer output was then analog filtered at 30 kHz and digitized at a rate of 60 kHz for 120 s long samples using a 16-bit data acquisition system (National Instruments PCI-6123). Probe calibrations were performed in-situ directly prior to measurement runs in the channel itself using a Pitot probe located at the channel centerline connected to a NIST calibrated pressure transducer (Omega PX-653). Measured bridge voltages were then corrected for any temperature fluctuations[12] as measured by a thermistor probe located in the tunnel (Omega THX-400) and a fourth order polynomial used to fit the calibration curves. This process leads to an estimated uncertainty of 2.2% in the mean velocity and 3.0% in the streamwise Reynolds stress. To capture the wall-normal streamwise velocity profile, the probes were mounted on a microstepping traverse. For the rough walled cases, the probes were traversed into the wall and destroyed to ensure accurate capture of the wall position and to provide measurements from within the roughness layer.

Measurements have been conducted at a single Reynolds number of $R_{e_h} = 35,000$ at four values of BR corresponding to 0%, 0.15%, 0.25%, and 0.37%. These results were compared to two sets of data from

the same facility with the smooth-walled surface in place. Smooth data set "A" matches the free-stream velocity of the test cases, $U_{cl} = 10.5m/s$, and smooth data set "B" matches the friction Reynolds number, $R_{e_\tau} = hu_\tau/\nu$, where $u_\tau = \sqrt{\tau_w \rho^{-1}}$ is the friction velocity . For the smooth wall data sets, the friction velocity was determined by performing a simple momentum balance[29] in the channel whereby

$$u_\tau = \left[(1/\rho)\epsilon_T \frac{h}{2}\frac{dp}{dx} \right]^{1/2} . \tag{3}$$

Here ϵ_T is a three-dimensionality factor equal to unity for flow in channels with sufficiently high aspect ratios[17] and dp/dx is the measured pressure gradient. Due to lack of a suitable alternative, the Clauser chart method was used to find the friction velocities of the rough walled cases.[7]

II. Results

A rough surface geometry can be characterized in numerous ways.[21] However the specific influence of each geometrical surface element on the mean flow quantities is difficult to determine. Present in table 1 are a few of the defining attributes which have been found for this set of experiments. As indicated by the values in table 1, the skin friction coefficient, $c_f = \tau_w/(\frac{1}{2}\rho U_{cl}^2)$, for the rough surface was approximately double that of the smooth-walled cases. As higher values of c_f indicate faster shear layer growth,[2] the increase in c_f with increasing BR suggests that the blowing acts to promote this shear layer growth.

Wall Type	U_{cl}(m/s)	$R_{e_h} \times 10^{-3}$	u_τ (m/s)	$R_{e_\tau} \times 10^{-3}$	$c_f \times 10^3$
Smooth A	10.48	35.23	0.44	1.48	3.5
Smooth B	16.91	56.85	0.68	2.29	3.2
Rough, $BR = 0\%$	10.46	35.16	0.63	2.12	7.2
Rough, $BR = 0.15\%$	10.59	35.60	0.66	2.22	7.7
Rough, $BR = 0.25\%$	10.33	34.73	0.68	2.29	8.4
Rough, $BR = 0.35\%$	10.62	35.71	0.72	2.42	9.2

Table 1. *Summary of boundary layer parameters for smooth and rough wall runs*

II.A. Mean Flow Characteristics

| Wall Type	d (μ m)	ΔU^+	k^+	k_s (μm)
Rough, $BR = 0\%$	287	7.82	11.9	2.9
Rough, $BR = 0.15\%$	370	8.42	12.4	3.5
Rough, $BR = 0.25\%$	145	9.42	12.8	5.1
Rough, $BR = 0.35\%$	159	10.22	13.6	6.5

Table 2. *Roughness and blowing characteristics*

Studies on rough wall turbulent boundary layers indicate that a shift of the turbulence producing shear layer above the surface occurs with increasing roughness height Reynolds number, here defined as $k^+ = k_{rms}u_\tau/\nu$ where k_{rms} is the rms roughness height.[2,4,11,21] This shift, d, is referred to as the zero-plane displacement.[24] In these experiments the value of d was determined by the offset of the region of near-zero streamwise Reynolds stress measured under conditions of roughness and blowing. For the remainder of this paper, wall normal distance is presented as $Y = y - d$, where y is the physical distance from the wall. The different values of d used are provided in table 2.

Also provided in table 2 is the roughness Reynolds number k^+, and the equivalent sand-grain roughness height, k_s, as defined by Raupach[24] for example. The flow regime was limited to the transitional, $5 < k^+ < 70$. Interestingly, we see that the effects of additional momentum injection act through an increase in the effective roughness height and a corresponding increase in local wall shear stress.

In Fig. 3 the mean velocity profiles, $U(Y)$, are presented using different normalizations. In Fig. 3(a) and (b), the profiles are compared using bulk properties h and U_{cl} for normalization, which illustrates the
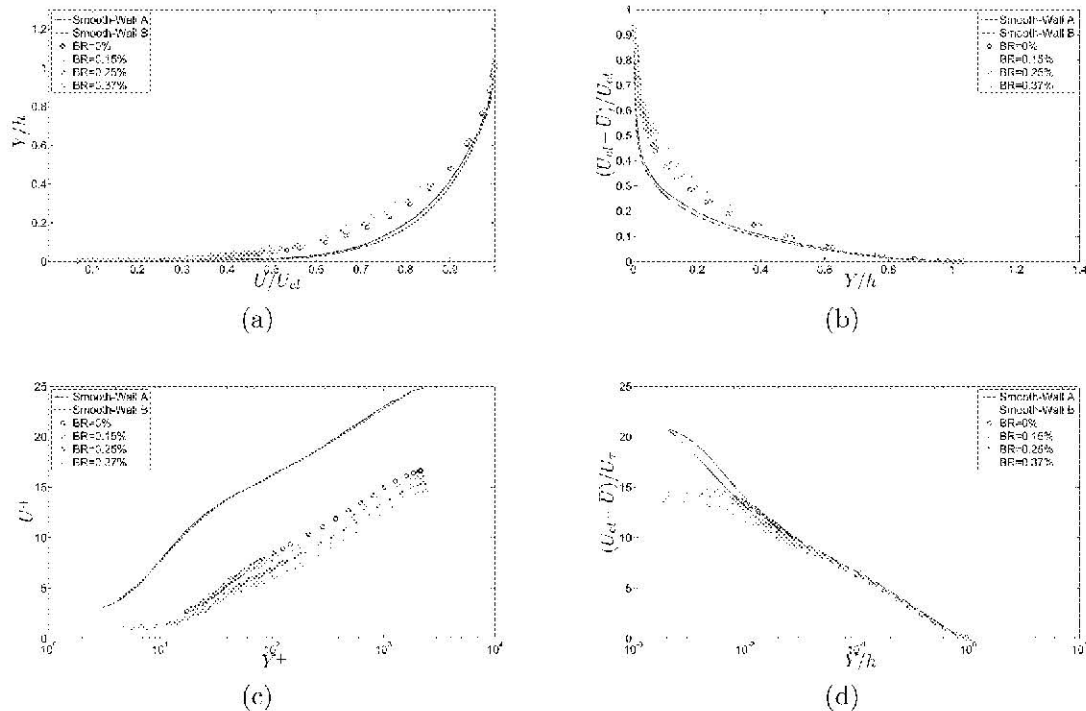
Figure 3. *Mean velocity profiles non-dimensionalized using (a) bulk properties, (b) velocity deficit using bulk properties, (c) inner scaling and (d) outer scaling.*

expected trend of the roughness and blowing making the profiles "less full" compared with the smooth wall case and it is evident that the effects of roughness are evident throughout the entire wall layer.

The mean velocity profiles shown in inner scaling where $U^+ = U/u_\tau$ and $Y^+ = Yu_\tau/\nu$ verify that one of the most interesting results observed in compressible flow[28] were also evident in incompressible flow. Namely, these results show that the mean velocity profile follows

$$U^+ = \kappa^{-1} \ln Y^+ + B - \Delta U^+(k^+) + \Pi \kappa^{-1} W(Y/h) \tag{4}$$

as illustrated in Fig. 3(c). Here κ is the von Kàrmàn constant, B an additive constant, $\Pi\kappa^{-1}W(y/h)$ the wake function. Note that this scaling is driven by the wall shear stress, τ_w. The effects of roughness on the mean flow are typically contained within the roughness function, $\Delta U^+(k^+)$,[21] which is itself dependent on the roughness Reynolds number, k^+. The estimated values of the ΔU^+ for each case are provided in table 2.

The profiles shown in Fig. 3(c) demonstrate that the momentum injection through the surface can be treated as a modification to ΔU^+, suggesting an analogy between momentum injection ratio, $BR = (\rho U)_{inj}/(\rho U)_{cl}$, and increased roughness height. Further support for this observation is found in the outer scaled profiles shown in Fig. 3(e) where collapse of all profiles is demonstrated for $Y/h > 0.1$, the outer layer of the flow. Hence the effects of additional blowing are consistent with Townsend's[27] hypothesis in that, sufficiently far from the surface, the effects of roughness on the flow are confined to those caused by the modification of the wall shear stress. Note that, support for this argument is somewhat tenuous with the present data set since here the wall shear stress was determined via the Clauser chart method, which necessarily assumes the validity of Eq. 4.

II.B. Streamwise Reynolds Stress

Profiles of the streamwise Reynolds stress, $\overline{u'^2}$, are presented normalized using outer coordinates in Fig. 4 (a) and in inner coordinates in Fig. 4 (b), where $u^{2+} = \overline{u'^2}/u_\tau^2$. In both scalings, collapse of the rough-wall data for all values of BR can be observed in the outer layer, although the smooth-walled profiles do not
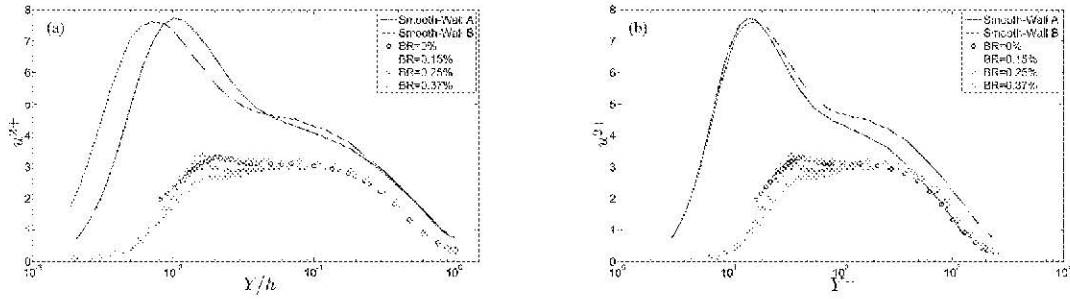
American Institute of Aeronautics and Astronautics

Figure 4. *Wall-normal profiles of streamwise Reynolds stress shown in (a) outer scaling and (b) inner scaling.*

collapse with those of the rough surface. Closer to the surface, we observe an inner peak in wall shear stress for the rough-walled cases, similar to that of the smooth-walled case but with reduced magnitude. As the roughness Reynolds number increases, viscous forces are dominated by drag inducing pressure forces resulting in the observed decrease in the magnitude of the near wall peak.

For the rough-walled cases, the location of the inner peak is shifted away from the wall, representing the shift in turbulence production towards taking place in separated shear layers forming over the surface of the roughness elements. It can also be noted that neither scaling results in collapse of the inner peak of the Reynolds stress with changing BR, with the magnitude of inner peak decreasing with increasing BR. This is consistent with the behavior expected due to increasing k^+ and therefore provides further support for the effect of additional momentum injection acting as an increase the effective roughness height.

II.C. Streamwise Power Spectra

Further insight into the modifications made to the spatial organization of the turbulence can be gained by examining the power spectrum. Here, this was performed using pre-multiplied spectral maps, as described in Hutchins and Marusic.[19] To produce these maps, for each wall-normal position time series data were processed using a Fast-Fourier Transform (FFT) to generate the streamwise power spectral density (PSD), $\phi_{uu}(f, Y)$ and converted to wavenumber space using Taylor's hypothesis, $\phi_{uu}(k_x, Y)$ where $k_x \approx 2\pi f/U$. The PSD was then pre-multiplied by the wavenumber to produce $k_x\phi_{uu}$. These premultiplied spectra were combined and are presented as spectral maps in Fig. 5, which have been normalized to show $k_x\phi_{uu}(\lambda/h, Y/h)/u_\tau^2$ where $\lambda = 2\pi/(k_x)$. Figures 5(a)-(e) therefore present the wavelength dependence of the contributions to the Reynolds stress, profiles of which are also included in Fig. 5 to better visualize which eddy wavelengths contribute to features observed in the Reynolds stress profiles. In particular, the results presented in Fig. 5 highlight the correlation between the near-wall peak of turbulence production in the Reynolds stress profiles and the corresponding peak (i.e. inner-energy site or near-wall signature) in the spectra, occurring at roughly $\lambda/h = 0.1$ and $Y/h = 0.01$. To better compare the differences between the smooth-walled and rough-walled cases, the location of the near-wall peak in the pre-multiplied spectrum has been marked with a ($+$) for the smooth-wall case and an (x) for the blowing cases.

For the smooth-walled case, the near-wall peak occurs at $Y/h = 0.006$ ($Y^+ = Yu_\tau/\nu = 13.7$) and $\lambda/h = 0.5$ ($\lambda^+ = \lambda u_\tau/\nu = 1143$). For the rough wall and blowing cases, as well as the previously observed shift in the peak away from the wall and decrease in magnitude of near wall peak, it is also evident that the roughness also shifts the near-wall energy containing signature from wavelengths of $\lambda \approx 0.6h$ to $\lambda \approx 0.2h$, which is approximately twice the streamwise wavelength of the roughness elements. This reflects a shift in turbulence production mechanism towards one driven by roughness geometry. Compared to the $BR = 0$ case, a continual decrease in the near-wall energy content is observed with increasing BR. This points to increased disruption of the near-wall turbulence production cycle present across multiple small wavelengths that scale with the roughness height of 1 mm. However, despite experiencing a reduction in magnitude, the wavelengths and wall-normal location of the near-wall peak appears stationary across all blowing rates.

Also present in the spectral contours, extending out towards the larger wavelengths are the double humps or "dominant energy modes" as identified by, for example, Monty et al.[18] These modes have been established as the large and very-large scale motions (LSMs and VLSMs).[8-10,13,39] The formation of LSMs

American Institute of Aeronautics and Astronautics

(a) Smooth Wall Case B

(b) Rough, BR=0 %

(c) Rough, BR=0.15%
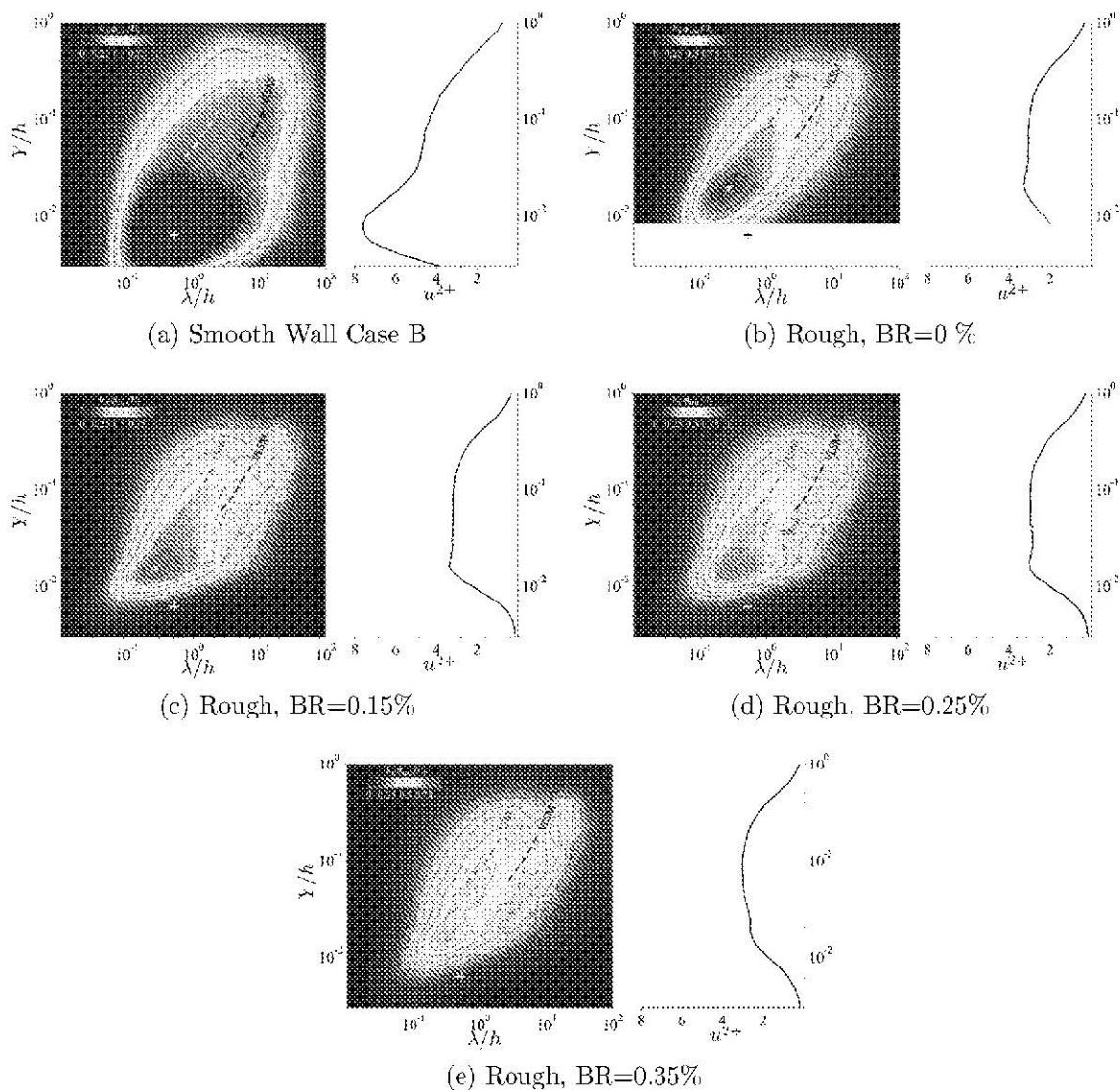
(d) Rough, BR=0.25%

(e) Rough, BR=0.35%

Figure 5. *Pre-multiplied power spectral density plots, contour colors indicate the magnitude of $k_x \phi_{uu}/u_\tau$*

is thought to relate to the alignment of so-called "hairpin" vortices into packets. These packets exist in a heirarchy of larger, older LSMs and smaller younger LSMs.[1] Furthermore, very long meandering regions of low momentum fluid have been observed in channel and pipe flow,[3,19] referred to as "superstructures" or VLSMs. These two modes have been hypothesized to contain as much as half the kinetic energy of the flow[8] and are therefore potentially important flow structures. The LSM and VLSM signatures have been identified with dashed lines in figure 5 and are observed in all cases. Although the energy content of the entire spectrum of the rough-walled cases, appears reduced relative to smooth-walled case (due to the increase in skin friction relative as observed in other studies on roughness)[4,11,21] the wavelengths of the LSM and VLSM appear relatively unchanged, with momentum injection appearing to produce no additional modification to the LSM and VLSM energy content.

To better compare the modifications to the energy content of the turbulence made by the momentum injection energy of the various blowing rates were generate we compare the difference between the three blowing rates and the baseline no blowing case, $BR = 0\%$, by subtracting the spectral contour map Fig. 5(b) from Fig. 5 (c)-(e). The results are presented in Fig. 6(a)-(c) respectively and most noticeably highlight the changes made to the near-wall peak. These plots demonstrate that the decrease in energy content observed in the Reynolds stress profiles of Fig. 4 for all cases occurs at $\lambda \approx 0.15h$, which is remarkably close to the

wavelength of the roughness elements of $\lambda = 0.14$. Therefore, it appears that the blowing is removing energy from eddies formed by the roughness elements. Simultaneously, a corresponding increase in energy can be observed at wavelengths an order of magnitude higher, reflecting a shift in turbulence production to that occurring over longer wavelengths. This, once again, is consistent with the momentum injection acting as a modification of effective roughness geometry.

Interestingly, Fig. 6 also shows changes in the LSM and VLSM structure with blowing, not previously evident in Fig. 5. This change in structure appears to consist of a decrease in energy content of the LSM wavelengths and a corresponding increase in VLSM wavelengths. These results suggest that there could be subtle changes in the organization of these long wavelength modes towards longer wavelengths which corresponds to the shift in near wall peak towards longer wavelengths as well.

(a) $BR - 0.15\%$

(b) $BR - 0.25\%$

(c) $BR = 0.37\%$
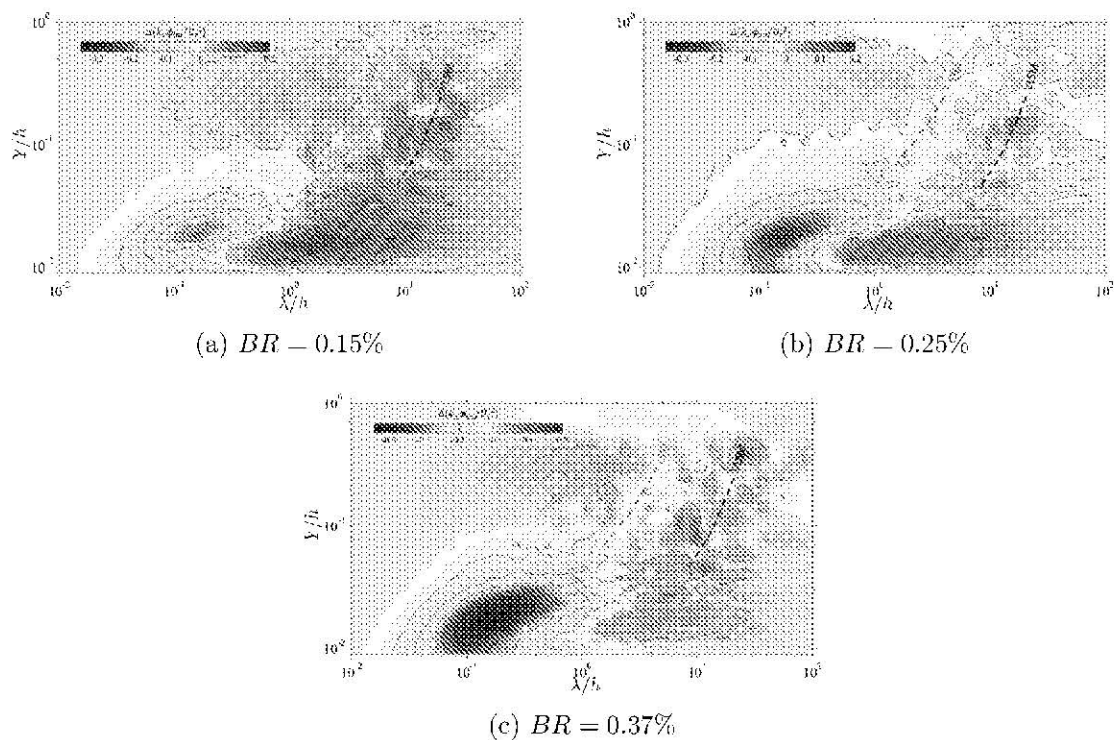
Figure 6. *Difference between energy spectra between rough-walled case with blowing and rough-walled cases without blowing,* $\Delta\, k_x \phi_{uu}/u_\tau]$.

III. Conclusions

Velocity measurements have been performed in turbulent channel flow investigating the combined effects of surface roughness and blowing. Scaling of the mean velocity profiles suggests that Townsend's hypothesis is supported even with momentum injection through the surface. Although comparison of the Reynolds stress profiles between the smooth-walled and rough-wall cases did not show collapse in the outer layer, additional the momentum injection appeared to indicate that the effects of momentum injection were confined to the near wall flow. The energy content of the near-wall turbulence was found to shift to wavelengths of the order of magnitude of the roughness elements for all rough-walled cases. The additional momentum injection was found to decrease energy content in wavelengths corresponding to the roughness elements, while simultaneously adding energy at longer wavelengths. The structure of the turbulence in the outer layer was found to be largely unchanged by the addition of momentum injection, although there was evidence of decreasing energy content in LSM modes and increasing energy content in VLSM modes.

The results are consistent in supporting the hypothesis that the effect of blowing could be modeled as a modification to the geometry through an increase in the height of the roughness elements. This support was observed through the additional displacement of the in inner-scaled mean velocity, the decreasing inner peak

magnitude in the Reynolds stress, and the shift in near-wall energy content towards longer wavelengths.

Acknowledgments

References

[1] Adrian, R. C., Meinhart, C. D., and Tomkins, C. D. Vortex organization in the outer region of the turbulent boundary layer. *J. Fluid Mech.*, 422:1–54, 2000.

[2] Akinlade, O., Bergstrom, D., Tachie, M., and Castillo, L. Outer flow scaling of smooth and rough wall turbulent boundary layers. *Experiments in Fluids*, 37:604–612, 2004.

[3] Bailey, S., Hultmark, M., Smits, A., and Schultz, M. Azimuthal structure of turbulence in high Reynolds number pipe flow. *J. Fluid Mech.*, 615:121–138, 2008.

[4] Bakken, O., Krogstad, P., Ashrafian, A., and Andersson, H. Reynolds number effects in the outer layer of the turbulent flow in a channel with rough walls. *Phys. Fluids*, 17, 2005.

[5] Bertin, J. J. and Cummings, R. M. Fifty years of hypersonics: where we've been, where we're going. *Progress in Aerospace Sciences*, 39.6:511–536, 2003.

[6] Castro, I. P. Rough-wall boundary layers: Mean flow universality. *J. Fluid Mech.*, 585:469–485, 2007.

[7] Clauser, F. The turbulent boundary layer. *Advanced Applied Mechanics*, 4:1–51, 1956.

[8] Guala, M., Hommema, S. E., and Adrian, R. J. Large-scale and very-large-scale motions in turbulent pipe flow. *J. Fluid Mech.*, 554:521–542, 2006.

[9] Head, M. R. and Bandyopadhyay, P. New aspects of turbulent boundary-layer structure. *J. Fluid Mech.*, 107:297–337, 1981.

[10] Hutchins, N. and Marusic, I. Large-scale influences in near-wall turbulence. *Phil. Trans. R. Soc. A*, 365:647–664, 2007.

[11] Jiménez, J. Turbulent flows over rough walls. *Annu. Rev. Fluid Mech.*, 36:173–196, 2004.

[12] Jørgensen, F. *How to measure turbulence with hot-wire anemometers-a practical guide.* Dantec Dynamics, P.O. Box 121, Tonsbakken 16-18, DK-2740 Skovlunde, Denmark, 01 2002.

[13] Kim, K. C. and Adrian, R. J. Very large-scale motion in the outer layer. *Phys. Fluids*, 11(2):417–422, 1999.

[14] Langelandsvik, L. I., Kunkel, G. J., and Smits, A. J. Flow in a commercial steel pipe. *J. Fluid Mech.*, 595(-1):323–339, 2008.

[15] Lee, J., Sung, H. J., and Krogstad, P. Direct numerical simulation of the turbulent boundary layer over a cube-roughened wall. *J. Fluid Mech.*, 669:397–431, 2011.

[16] McDonough, J., Yang, T., and Sheetz, M. Parallelization of a modern cfd incompressible turbulent flow code. *Parallel Computational Fluid Dynamics: Advanced Numerical Methods, Software, and Applications*, pages 473–479, 2004.

[17] Monty, J. P. *Developments in Smooth Wall Turbulent Duct Flows.* PhD thesis, University of Melbourne, 2005.

[18] Monty, J. P., Stewart, J. A., Williams, R. C., and Chong, M. Large-scale features in turbulent pipe and channel flows. *J. Fluid Mech.*, 589:147–156, 2007.

[19] Monty, J., Hutchins, N., Ng, H., Marusic, I., and Chong, M. A comparison of turbulent pipe, channel and boundary layer flows. *J. Fluid Mech.*, 632:431–442, 2009.

[20] Pope, S. B. *Turbulent Flows.* Cambridge University Press, 2000.

[21] Raupach, M. R., Antonia, R., and Rjagopalan, S. Rough-wall turbulent boundary layers. *Appl. Mech. Rev.*, 44:1–25, 1991.

[22] Reshotko, E. Boundary-layer stability and transition. *Annu. Rev. Fluid Mech.*, 8.1:311–349, 1976.

[23] Schneider, S. P. Hypersonic boundary-layer transition with ablation and blowing. *AIAA Paper 3730*, 2008.

[24] Schultz, R. V. M. and Flack, K. Turbulence structure in boundary layers over periodic two- and three-dimensional roughness. *J. Fluid Mech.*, 676:172, 2011.

[25] Shockling, M. A., Allen, J. J., and Smits, A. J. Roughness effects in turbulent pipe flow. *J. Fluid Mech.*,

American Institute of Aeronautics and Astronautics

564:267 285, 2006.

[26] Tavoularis, S. *Measurement in Fluid Mechanics*. Cambridge University Press, 2005.

[27] Townsend, A. A. *The Structure of Turbulent Shear Flow*. Cambridge University Press, Cambridge, UK, 1976.

[28] Voisinet, R. Influence of roughness and blowing on compressible turbulent boundary layer flow. Technical report, Naval Surface Weapons Center, White Oak Lab, Silver Spring, MD, June 1979.

[29] Zanoun, E. S., Durst, F., and II., N. Evaluating the law of the wall in two-dimensional fully developed turbulent channel flows. *Phys. Fluids*, 15:3079 3089, 2003.

[30] Zhou, J., Adrian, R. J., Balachandar, S., and Kendall, T. M. Mechanisms for generating coherent packets of hairpin vortices in channel flows. *J. Fluid Mech.*, 387:353–396, 1999.